Comparison of Different Designs of Synchronous Reluctance Machines with High-Anisotropy Rotors

Erich Schmidt, *Member*, *IEEE*

Abstract – **In terms of torque capability, power factor and efficiency, synchronous reluctance machines with high-anisotropy rotors represent an alternative to conventional induction machines. In particular, they have very robust rotors and can therefore operate at constant power in a wider field-weakening range. The paper discusses a comparison of the various machine concepts using an identical machine geometry by using finite element analyses. Experimental results obtained from two machine designs confirm the results of the numerical analyses.**

Keywords – **Two-axes inductances, Reluctance machine, Permanent magnet synchronous machine, Synchronous machine, Finite element analysis**

I. Introduction

In most inverter fed electrical drives, asynchronous induction machines, synchronous reluctance machines or permanent magnet excited synchronous machines are utilized. For an application in high-performance drives in particular with a wide field-weakening range, both types of synchronous machines are more favourable against induction machines. This is based on their inherent suitability for a position-sensorless control scheme and additionally their more robust rotor [1]–[7].

In order to achieve a comparable performance, synchronous reluctance machines should be equipped with a high-anisotropy rotor design with internal flux barriers [1], [3]–[5], [8]. In comparison to conventional synchronous reluctance machines, the effective saliency of such rotor designs can be increased by permanent magnets inserted into the flux barriers [9]–[12]. On the other hand, the permanent magnet excited synchronous machine can be realized with such a high-anisotropy rotor design and two different arrangements of the permanent magnets resulting in a complete different behaviour in particular within the field-weakening range.

Consequently, there are four different machine concepts which utilize identical stator and rotor geometries as well as identical winding data. The paper compares these four machine designs in terms of the operating behaviour in particular in the field-weakening region. In order to confirm the numerical results from various finite element analyses, measurement data from two rotor designs are presented additionally.

Erich Schmidt is with the Institute of Energy Systems and Electric Drives, Vienna University of Technology, Vienna, Austria (Email: erich.schmidt@tuwien.ac.at).

II. Space Vector Calculus

In the dq rotor fixed reference frame, the normalized stator current and stator flux space vectors are given by

$$\underline{i}_{S,dq} = i_S \; \mathrm{e}^{\jmath\beta} \; = i_{Sd} + \jmath\, i_{Sq} \;\; , \tag{1}$$

$$\underline{\psi}_{S,dq} = \psi_S \; \mathrm{e}^{\jmath\vartheta} = \psi_{Sd} + \jmath\, \psi_{Sq} \;\; . \tag{2}$$

Therein, i_S,ψ_S represent the magnitudes of stator current and stator flux, β,ϑ denote stator current angle and stator flux angle, respectively. By using direct and quadrature axis stator inductances l_d,l_q as well as the linkage flux of the permanent magnets ψ_M, the components of the stator linkage flux can be written as

$$\psi_{Sd} = l_d\, i_{Sd} + \psi_{Md} \;\; , \tag{3a}$$

$$\psi_{Sq} = l_q\, i_{Sq} + \psi_{Mq} \;\; . \tag{3b}$$

Consequently, the normalized electromagnetic torque is obtained from

$$\begin{aligned} t_i &= -\frac{3}{2}\, \mathrm{Im}\Big(\underline{i}^*_{S,dq}\, \underline{\psi}_{S,dq}\Big) = \frac{3}{2}\Big(\psi_{Sd}\, i_{Sq} - \psi_{Sq}\, i_{Sd}\Big) \\ &= \frac{3}{2}\, i_S^2 \left(\frac{\psi_{Md}}{i_S}\, \sin\beta - \frac{\psi_{Mq}}{i_S}\, \cos\beta + \frac{l_d - l_q}{2}\, \sin 2\beta\right) . \end{aligned} \tag{4}$$

The conventional reluctance machine can be described with a vanishing linkage flux $\psi_M = 0$. With the permanent magnet assisted reluctance machine, $\psi_{Mq} < 0$ represents the linkage flux of the permanent magnet which counteracts to any quadrature axis stator current $i_{Sq} > 0$. On the other hand, the permanent magnet excited reluctance machine with $\psi_{Md} > 0$ can be designed as either a normal-saliency machine $l_d > l_q$ or an inverse-saliency machine with $l_d < l_q$.

III. Machine Designs

Fig. 1 depicts the various arrangements of high-anisotropy rotors with internal rotor flux barriers:

a. conventional reluctance machine without any permanent magnets, normal-saliency $l_d > l_q$,

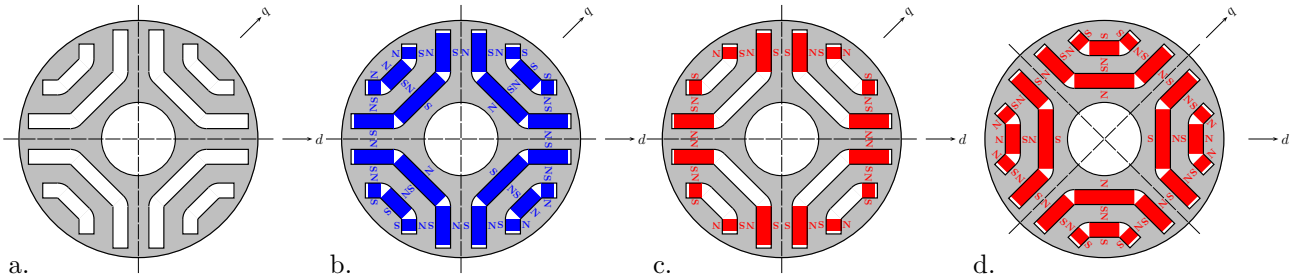

Fig. 1: Comparison of the machine designs: a. conventional reluctance machine, normal-saliency $l_d > l_q$, b. permanent magnet assisted reluctance machine with $\psi_{Mq} < 0$, normal-saliency $l_d > l_q$, c. permanent magnet excited reluctance machine with $\psi_{Md} > 0$, normal-saliency $l_d > l_q$, d. permanent magnet excited reluctance machine with $\psi_{Md} > 0$, inverse-saliency $l_d < l_q$

b. permanent magnet assisted reluctance machine with $\psi_{Mq} < 0$, normal-saliency $l_d > l_q$,
c. permanent magnet excited reluctance machine with $\psi_{Md} > 0$, normal-saliency $l_d > l_q$,
d. permanent magnet excited reluctance machine with $\psi_{Md} > 0$, inverse-saliency $l_d < l_q$.

Fig. 2 depicts the finite element model of stator and high-saliency rotor of the different machine designs concerned. With all four designs, the stator is identical and consists of 24 slots carrying a conventional star-connected three-phase full-pitch winding. Slot wedges with a magnetic anisotropy are utilized to minimize the cogging torque of the unskewed machine.

With regard to the circumferential symmetry, only one pole pitch is included in the finite element model. The various angular rotor positions are modelled with a concentric sliding surface inside the air-gap. This approach facilitates fully independent stator and rotor model parts without any remeshing of the air-gap regions when considering different angular rotor displacements [13]–[15].

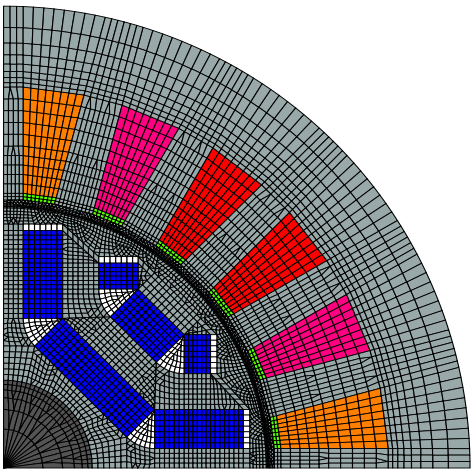

Fig. 2: Finite element model of stator and high-saliency rotor with a sliding surface inside the air-gap

The results discussed further on are evaluated from various finite element analyses. Thereby, the electromagnetic torque is obtained from the Maxwell stresses inside the air-gap [13], [16], [17]. On the other hand, the inductances presented in the following are always apparent inductances obtained by utilizing the frozen permeabilities method [16]–[18].

IV. Analysis Results

A. Comparison with Measurements

Fig. 3 and Fig. 4 depict a comparison of measurement data and numerical results for the electromagnetic torque from two designs, the permanent magnet assisted reluctance machine with $\psi_{Mq} = -0.30$ and

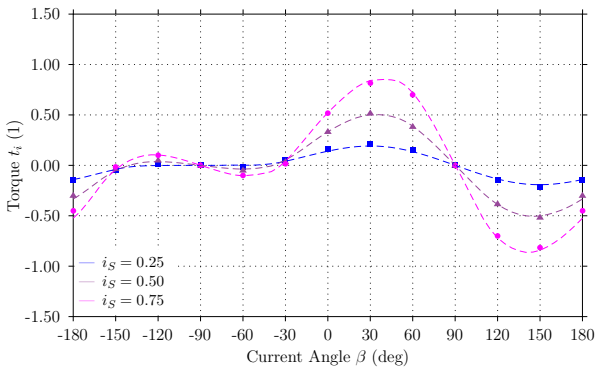

Fig. 3: Torque versus stator current angle β, comparison of numerical results (dashed line) and measurement data (symbols), PM assisted reluctance machine

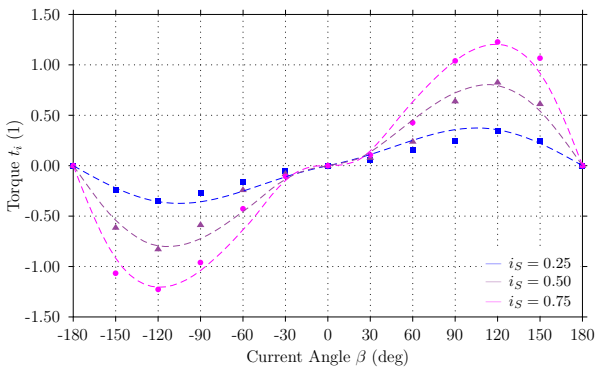

Fig. 4: Torque versus stator current angle β, comparison of numerical results (dashed line) and measurement data (symbols), inverse-saliency PM reluctance machine

the inverse-saliency permanent magnet excited reluctance machine with $\psi_{Md} = 0.66$. Obviously, there is a good agreement between the measurement data and the results obtained numerically.

B. Reluctance Machines

As from (4), for any given stator current i_S the maximum torque of the conventional reluctance machine is achieved with a current angle of $\cos 2\beta = 0$. On the other hand, for any given stator current i_S the maximum torque of the permanent magnet assisted reluctance machine is achieved with a current angle of

$$\sin\beta = \frac{\psi_{Mq}}{4\,(l_d - l_q)\,i_S} + \sqrt{\left(\frac{\psi_{Mq}}{4\,(l_d - l_q)\,i_S}\right)^2 + \frac{1}{2}}\ . \quad (5)$$

Fig. 5 shows the ratio l_d/l_q in dependence on the stator current magnitude i_S with various current angles. On the other hand, Fig. 6 depicts the absolute value of the power factor $\cos\varphi \approx \sin(\beta - \vartheta)$ in dependence on the stator current magnitude i_S with various current angles.

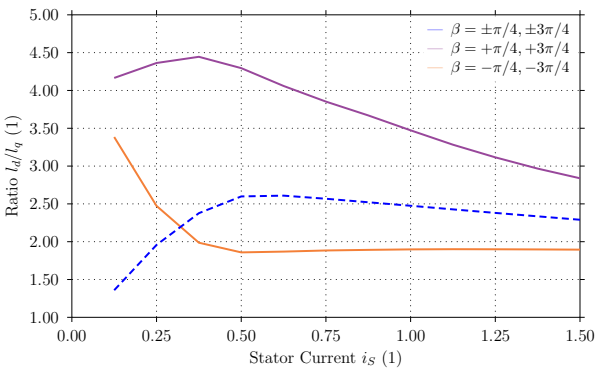

Fig. 5: Ratio l_d/l_q versus stator current magnitude i_S, current angles of $\beta = \pm\pi/4, \pm 3\pi/4$, conventional reluctance machine (dashed line), PM assisted reluctance machine (straight line)

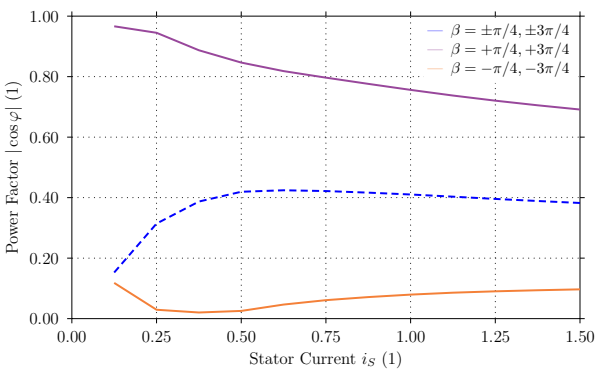

Fig. 6: Power factor $|\cos\varphi|$ versus stator current magnitude i_S, current angles of $\beta = \pm\pi/4, \pm 3\pi/4$, conventional reluctance machine (dashed line), PM assisted reluctance machine (straight line)

In comparison of both designs of the reluctance machine, the permanent magnet assisted reluctance machine yields the best performance at current angles as given by (5) nearby $\beta = \pi/4$ or $\beta = 3\pi/4$. Consequently, the permanent magnets with $\psi_{Mq} = -0.30$ significantly increase the ratio l_d/l_q of the apparent inductances yielding a wider speed range with constant power. Additionally, they result in an increased power factor with current angles of $\beta > 0$. With higher stator current magnitudes on the other hand, the saturation level increases which results in decreasing saliency-ratio and power factor.

Further, Fig. 7 and Fig. 8 depict the torque t_i with various stator current magnitudes. Finally, Fig. 9 and Fig. 10 show current trajectories resulting in a contour map of the torque t_i.

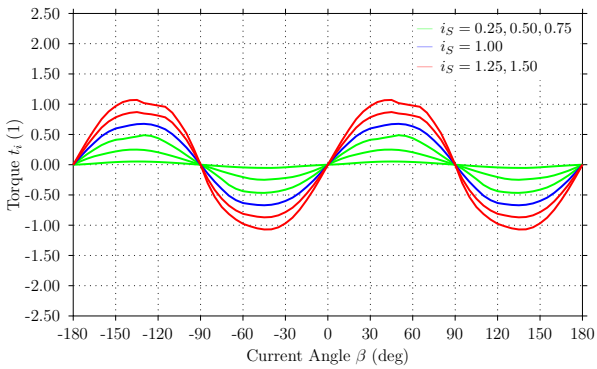

Fig. 7: Torque t_i versus stator current angle β, current magnitudes of $i_S = 0.25 \ldots 1.50$, conventional reluctance machine

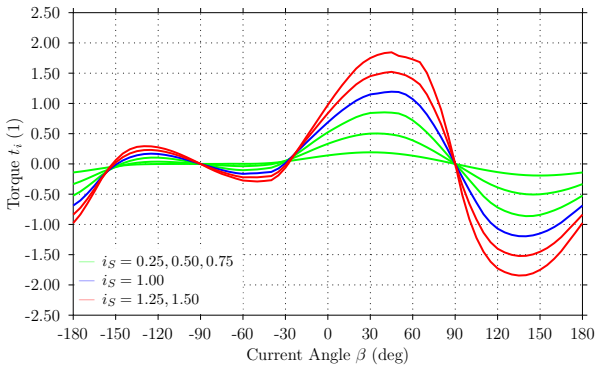

Fig. 8: Torque t_i versus stator current angle β, current magnitudes of $i_S = 0.25 \ldots 1.50$, PM assisted reluctance machine

Obviously, the compensation of the quadrature axis current accomplished by the permanent magnets significantly increases the evolved torque in the range of $0 \le \beta \le \pi$. In particular, the contour map Fig. 10 confirms the best performance of the permanent magnet assisted reluctance machine at current angles nearby $\beta = \pi/4$ or $\beta = 3\pi/4$.

C. Permanent Magnet Machines

As from (4), for any given stator current i_S in case of the normal-saliency machine the maximum torque

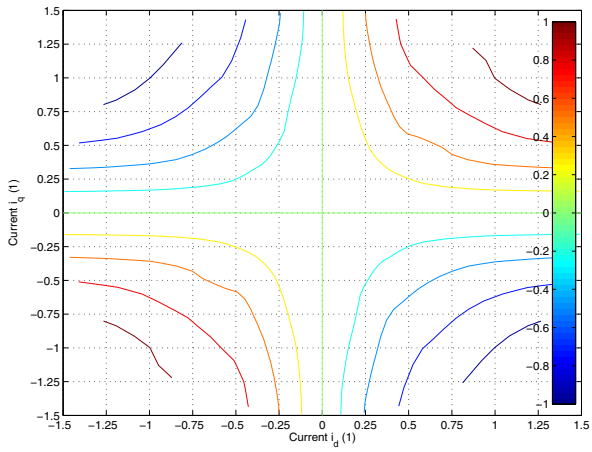

Fig. 9: Contour map of torque t_i versus stator current components i_d,i_q, conventional reluctance machine

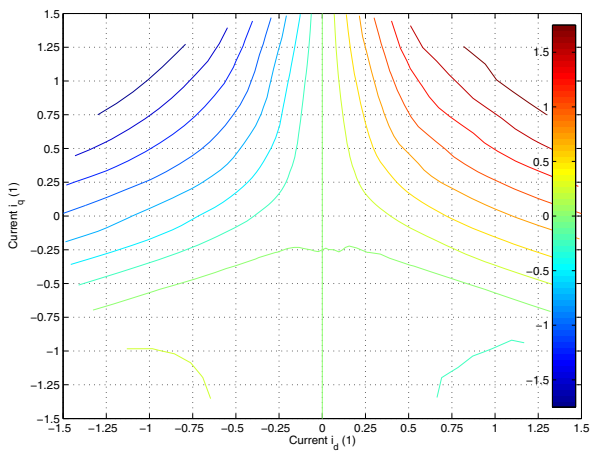

Fig. 10: Contour map of torque t_i versus stator current components i_d,i_q, PM assisted reluctance machine

of the is achieved with a current angle of

$$\cos\beta = -\frac{\psi_{Md}}{4\,(l_d - l_q)\,i_S} + \sqrt{\left(\frac{\psi_{Md}}{4\,(l_d - l_q)\,i_S}\right)^2 + \frac{1}{2}} \quad (6)$$

and in case of the inverse-saliency machine

$$\cos\beta = -\frac{\psi_{Md}}{4\,(l_d - l_q)\,i_S} - \sqrt{\left(\frac{\psi_{Md}}{4\,(l_d - l_q)\,i_S}\right)^2 + \frac{1}{2}}\,. \quad (7)$$

Fig. 11 shows the ratio l_d/l_q of the normal-saliency machine and the ratio l_q/l_d of the inverse-saliency machine with $\psi_{Md} = 0.66$ in dependence on the stator current magnitude i_S with various current angles. On the other hand, Fig. 12 depicts the absolute value of the power factor $\cos\varphi \approx \sin(\beta - \vartheta)$ in dependence on the stator current magnitude i_S with various current angles.

In comparison of both designs of the permanent magnet excited machine, the inverse-saliency permanent machine yields a significantly increased power factor in particular with current angles of $\pi/2 \leq \beta \leq 3\pi/4$ representing the regular operational mode with a

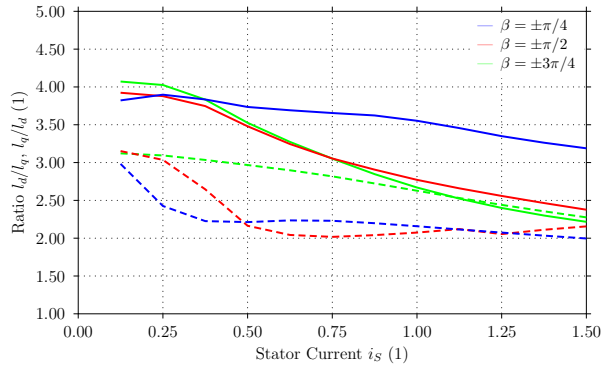

Fig. 11: Ratio l_d/l_q or l_q/l_d versus stator current magnitude i_S, current angles of $\beta = \pm\pi/4, \pm\pi/2, \pm 3\pi/4$, normal-saliency PM reluctance machine (dashed lines), inverse-saliency PM reluctance machine (straight lines)

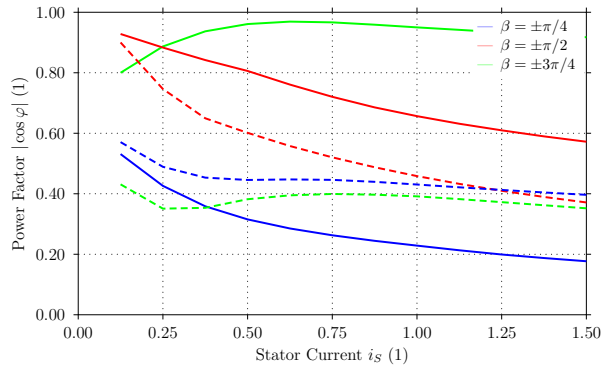

Fig. 12: Power factor $|\cos\varphi|$ versus stator current magnitude i_S, current angles of $\beta = \pm\pi/4, \pm\pi/2, \pm 3\pi/4$, normal-saliency PM reluctance machine (dashed lines), inverse-saliency PM reluctance machine (straight lines)

quadrature current only as well as the field-weakening region. On the other hand, the inverse-saliency permanent magnet machine shows the highest saliency-ratio of the apparent inductances yielding the widest speed range with constant power. In particular, an operation at current angles nearby $\beta = \pi/4$ results in a high saliency-ratio but simultaneously a poor power factor. Again with higher stator current magnitudes, the saturation level increases which results in decreasing saliency-ratio and power factor.

Further, Fig. 13 and Fig. 14 depict the torque t_i with various stator current magnitudes. Finally, Fig. 15 and Fig. 16 show current trajectories resulting in a contour map of the torque t_i.

Obviously, the normal-saliency machine acts rather like a reluctance machine due to the high saturation occurring from the flux concentration in the direct axis. The contour map Fig. 15 confirms this behaviour quite well. Therefore, this arrangement does not present a significant improvement against the arrangement without permanent magnets.

On the other hand, the contour map Fig. 16 confirms the behaviour of the inverse-saliency permanent magnet machine where a given torque value can be obtained with only a quadrature current but equally

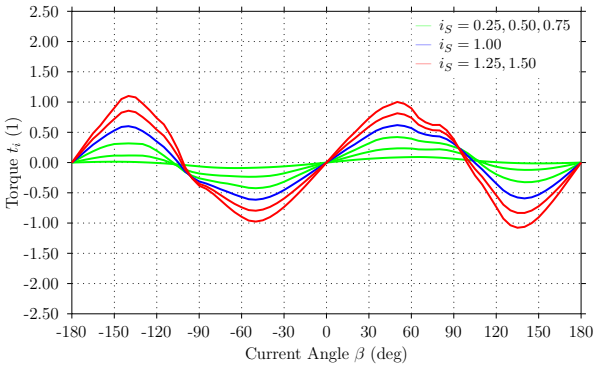

Fig. 13: Torque t_i versus stator current angle β, current magnitudes of $i_S = 0.25 \ldots 1.50$, normal-saliency PM reluctance machine

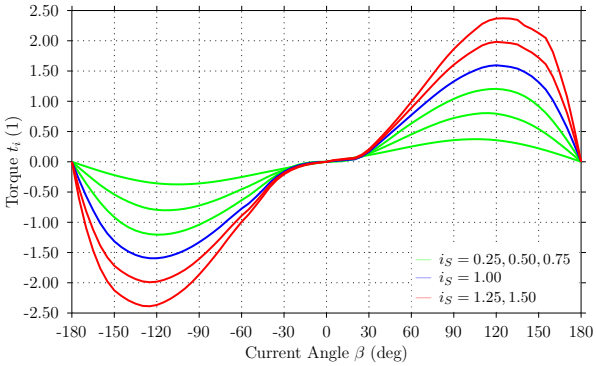

Fig. 14: Torque t_i versus stator current angle β, current magnitudes of $i_S = 0.25 \ldots 1.50$, inverse-saliency PM reluctance machine

with a smaller current within the field-weakening region yielding an increased efficiency due to the reduced power losses.

Further, the inverse-saliency permanent magnet machine can operate on the current limit in a wide speed range. Due to the rather small apparent inductance in direct axis, such a machine can produce much higher torque values without demagnetizing the permanent magnets in case of an increased current limit of the inverter. Consequently, the inverse-saliency machine shows an inherent suitability for electrical drives where short overload operational conditions require high torque values.

V. Conclusion

Synchronous reluctance machines with internal rotor flux barriers are well suited for an application in position-sensorless drives with a wide field-weakening range due to their high effective saliency. By using an identical machine geometry, the conventional reluctance machine and the permanent magnet assisted reluctance machine as well as the normal-saliency permanent magnet machine and the inverse-saliency permanent magnet machine are compared against their operational behaviour in particular in the field-weakening range.

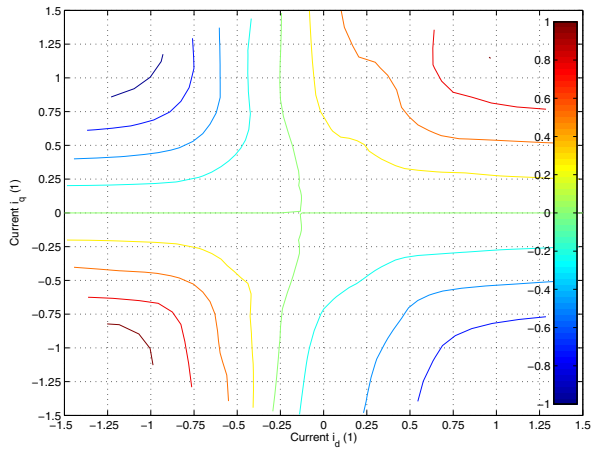

Fig. 15: Contour map of torque t_i versus stator current components i_d,i_q, normal-saliency PM reluctance machine

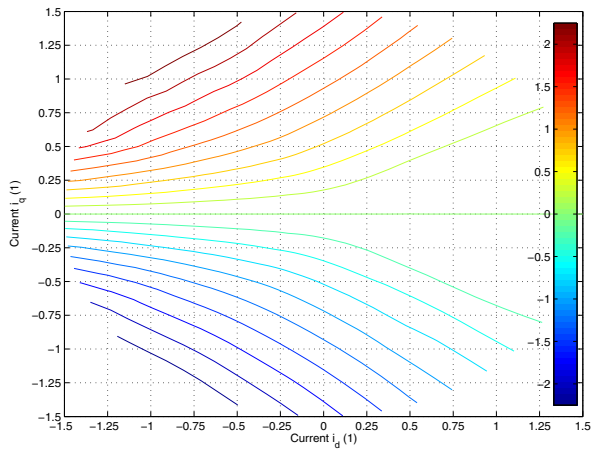

Fig. 16: Contour map of torque t_i versus stator current components i_d,i_q, inverse-saliency PM reluctance machine

The comparison is done in terms of current trajectories with respect to the dq reference frame according to current and voltage limits of the inverter. These diagrams obviously show the advantages of a high saliency ratio l_d/l_q in case of normal-saliency machines or l_q/l_d in case of inverse-saliency machines in particular in the field-weakening region. Thereby, the results from the finite element analyses are successfully compared with measurement data obtained from two machine designs.

References

[1] Vagati A., Fratta A., Franceschini G.: "AC Motors for High-Performance Drives: A Design-Based Comparison". *IEEE Transactions on Industry Applications*, Vol. 32, No. 5, September 1996.

[2] Miller J.M., McClear P.J., Lang J.H.: "Starter-Alternator for Hybrid Electric Vehicle: Comparison of Induction and Variable Reluctance Machines and Drives". *Proceedings of the IEEE Industry Applications Society 33th Annual Meeting*, St.Louis (MO, USA), 1998.

[3] Lovelace E.C., Jahns T.M., Lang J.H.: "Impact of Saturation and Inverter Cost on Interior PM Synchronous Machines Drive Optimization". *IEEE Transactions on Industry Applications*, Vol. 36, No. 3, May 2000.

[4] Vagati A., Pastorelli M., Scapino F., Franceschini G.: "Impact of Cross Saturation in Synchronous Reluctance Motors of the Transverse-Laminated Type". *IEEE Transactions on Industry Applications*, Vol. 36, No. 4, July 2000.

[5] Vagati A., Canova A., Chiampi M., Pastorelli M., Repetto M.: "Design Refinement of Synchronous Reluctance Motors Through Finite Element Analysis". *IEEE Transactions on Industry Applications*, Vol. 36, No. 4, July 2000.

[6] Haataja J., Pyrhönen J.: "Synchronous Reluctance Motor: An Alternative to Induction Motor". *Proceedings of the 14th International Conference on Electrical Machines, ICEM*, Espoo (Finland), 2000.

[7] De Kock H.W., Kamper M.J., Kennel R.M.: "Anisotropy Comparison of Reluctance and Permanent Magnet Synchronous Machines for Low Speed Position Sensorless Applications". *Proceedings of the 13th Power Electronics and Motion Control Conference, EPE-PEMC*, Poznan (Poland), 2008.

[8] Bianchi N., Bolognani S., Chalmers B.J.: "Comparison of Different Synchronous Motors Drives for Flux-Weakening Applications". *Proceedings of the 13th International Conference on Electric Machines, ICEM*, Instanbul (Turkey), 1998.

[9] Weinmeier P.: *Lagegeberlose hochdynamische Regelung eines Hybrid-Reluktanzmotors im unteren Drehzahlbereich bis zum Stillstand*. Doctoral Thesis (in German), Vienna University of Technology, 1998.

[10] Lee J.H., Kim J.C., Hyun D.S.: "Effect Analysis of Magnet on L_d and L_q Inductance of Permanent Magnet Assisted Synchronous Reluctance Motor using Finite Element Method". *IEEE Transactions on Magnetics*, Vol. 35, No. 3, May 1999.

[11] Schmidt E., Brandl W., Grabner C.: "Design Improvement of Synchronous Reluctance Machines with Internal Rotor Flux Barriers for High-Speed Drives". *Proceedings of the 33rd IEEE Power Electronics Specialists Conference, PESC*, Cairns (QLD, Australia), 2002.

[12] Bianchi N., Bolognani S., Bon D., Dai Pré M.: "Rotor Flux-Barrier Design for Torque Ripple Reduction in Synchronous Reluctance and Permanent Magnet Assisted Synchronous Reluctance Motors". *IEEE Transactions on Industry Applications*, Vol. 45, No. 3, May 2009.

[13] Hameyer K., Belmans R.: *Numerical Modelling and Design of Electrical Machines and Devices*. WIT Press, Southampton (UK), 1999.

[14] De Gersem H., Gyselinck J., Dular P., Hameyer K., Weiland T.: "Comparison of Sliding Surface and Moving Band Techniques in Frequency-Domain Finite Element Models of Rotating Machines". *Proceedings of the 6th International Workshop on Electric and Magnetic Fields (EMF)*, Aachen (Germany), 2003.

[15] De Gersem H., Weiland T.: "Harmonic Weighting Functions at the Sliding Surface Interface of a Finite Element Machine Model Incorporating Angular Displacement". *IEEE Transactions on Magnetics*, Vol. 40, No. 2, March 2004.

[16] Bastos J.P.A., Sadowski N.: *Electromagnetic Modeling by Finite Element Methods*. Marcel Dekker Ltd, New York (USA), 2003.

[17] Bianchi N.: *Electrical Machine Analysis Using Finite Elements*. CRC Press, Boca Raton (USA), 2005.

[18] Walker J.A., Dorrell D.G., Cossar C.: "Flux Linkage Calculation in Permanent Magnet Motors Using the Frozen Permeabilities Method". *IEEE Transactions on Magnetics*, Vol. 41, No. 10, October 2005.

Erich Schmidt was born in Vienna, Austria, in 1959. He received his MSc and PhD degrees in Electrical Engineering from the Vienna University of Technology, Austria, in 1985 and 1993, respectively. Currently, he is an Associate Professor of Electrical Machines at the Institute of Energy Systems and Electric Drives of the Vienna University of Technology. His research and teaching activities are on numerical field computation techniques and design optimization of electrical machines and transformers. He has authored more than 100 technical publications mainly in the fields of electrical machines and numerical field calculation.